Atmospheric boundary layer classification with Doppler lidar

Article

Published Version

Journal of Geophysical Research: Atmospheres

RESEARCH ARTICLE
10.1029/2017JD028169

Atmospheric Boundary Layer Classification With Doppler Lidar

A. J. Manninen[1], T. Marke[2], M. Tuononen[1,3,4], and E. J. O'Connor[3,5]

[1]Department of Physics, University of Helsinki, Helsinki, Finland, [2]Institute for Geophysics and Meteorology, University of Cologne, Cologne, Germany, [3]Finnish Meteorological Institute, Helsinki, Finland, [4]Vaisala Oyj, Vantaa, Finland, [5]Department of Meteorology, University of Reading, Reading, UK

A. J. Manninen and T. Marke contributed equally to this work.

Key Points:
- Atmospheric boundary layer classification method objectively assigns a source for the turbulent mixing identified by Doppler lidar
- The site-independent method outputs a pixel-based classification for the turbulent source at high temporal and spatial resolution
- The method requires only Doppler lidar measurements but can be extended to use supplementary information as well

Correspondence to:
A. J. Manninen,
antti.j.manninen@helsinki.fi

Citation:
Manninen, A. J., Marke, T., Tuononen, M. J., & O'Connor, E. J. (2018). Atmospheric boundary layer classification with Doppler lidar. *Journal of Geophysical Research: Atmospheres*, *123*, 8172–8189. https://doi.org/10.1029/2017JD028169

Received 7 DEC 2017
Accepted 22 JUN 2018
Accepted article online 29 JUN 2018
Published online 6 AUG 2018

Abstract We present a method using Doppler lidar data for identifying the main sources of turbulent mixing within the atmospheric boundary layer. The method identifies the presence of turbulence and then assigns a turbulent source by combining several lidar quantities: attenuated backscatter coefficient, vertical velocity skewness, dissipation rate of turbulent kinetic energy, and vector wind shear. Both buoyancy-driven and shear-driven situations are identified, and the method operates in both clear-sky and cloud-topped conditions, with some reservations in precipitation. To capture the full seasonal cycle, the classification method was applied to more than 1 year of data from two sites, Hyytiälä, Finland, and Jülich, Germany. Analysis showed seasonal variation in the diurnal cycle at both sites; a clear diurnal cycle was observed in spring, summer, and autumn seasons, but due to their respective latitudes, a weaker cycle in winter at Jülich, and almost non-existent at Hyytiälä. Additionally, there are significant contributions from sources other than convective mixing, with cloud-driven mixing being observed even within the first 500 m above ground. Also evident is the considerable amount of nocturnal mixing within the lowest 500 m at both sites, especially during the winter. The presence of a low-level jet was often detected when sources of nocturnal mixing were diagnosed as wind shear. The classification scheme and the climatology extracted from the classification provide insight into the processes responsible for mixing within the atmospheric boundary layer, how variable in space and time these can be, and how they vary with location.

1. Introduction

Reliable representation of turbulent mixing within the atmospheric boundary layer (ABL) is essential for air quality studies, wind energy, and for weather and climate models (e.g., Garratt, 1994). Turbulent mixing is responsible for the redistribution of momentum, mass, temperature, and humidity within the ABL (Oke, 1992). In addition, turbulent processes govern the rate of exchange between the surface and the atmosphere and determine the transport of aerosol away from the surface (Fuentes et al., 2016; Kaimal & Finnigan, 1994). The sources of turbulent mixing include buoyancy production and wind shear production (Deardorff, 1972; Moeng & Sullivan, 1994) and are highly variable in time and space; therefore, accurate measurements (Baklanov et al., 2011) and representation in numerical models are a challenge (Holtslag et al., 2013).

Buoyancy production, in terms of surface-driven convective mixing, is usually the dominant source of turbulent mixing in the ABL during the day (Oke, 1992), and also, radiative cooling in stratocumulus layers can drive top-down mixing from the cloud layer toward the surface during day and night (Hogan et al., 2009; Wood, 2012). Shear-driven production arises from shear in the near-surface wind profile induced by mechanical friction between the atmosphere and surface and from the shear associated with low-level jets (e.g., Banta et al., 2006; Tuononen et al., 2017).

Doppler lidar measurements provide sufficient temporal and spatial resolution for observing turbulent mixing in the ABL (e.g., Tucker et al., 2009) but have typically concentrated on particular quantities (O'Connor et al., 2010; Smalikho & Banakh, 2017; Vakkari et al., 2015) or processes (Barlow et al., 2011; Hogan et al., 2009; Su et al., 2016; Träumner et al., 2011) or deriving the mixing level height (Baars et al., 2008; Emeis et al., 2008; Pearson et al., 2010; Schween et al., 2014). To better comprehend the complex structure and evolution of the ABL, Harvey et al. (2013) introduced a profile-based Doppler lidar method for determining specific ABL types concentrating on whether the cloud-topped ABL was coupled to the surface.

Here we introduce a method that builds upon the method presented by Harvey et al. (2013) and which objectively assigns a source for the turbulent mixing identified in the ABL by Doppler lidar. The method combines

Table 1
Instrument Parameters During Standard Operation for the Halo Lidar at Hyytiälä (Jülich)

Parameter	Value
Wavelength	1.5 μm
Detector	Heterodyne
Pulse repetition frequency	15 kHz
Nyquist velocity	Approximately 20 m/s
Sampling frequency	50 MHz
Velocity resolution	0.038 m/s
Telescope	Monostatic optic-fiber coupled
Range resolution	30 m
Pulse duration	0.2 (0.15) μs
Lens diameter	8 (7.5) cm
Lens divergence	33 μrad
Minimum range	90 m
Maximum range	9,600 (8,400) m
Points per range bin	10

multiple quantities derived from Doppler lidar measurements to output a pixel-based classification for the turbulent source at high temporal and spatial resolution (3 min and 30 m for the instruments used here). The method is robust for almost all situations except fog and precipitation and is intended to be site independent. Fog often impedes the propagation of the Doppler lidar signal and is mostly present at elevation, which are lower than the lowest observable Doppler lidar range gate 105 m. Contamination of lidar measurements from precipitation can be an issue, and the methodology could be improved with an inclusion of a robust method for detecting precipitation in Doppler lidar measurements which to the authors' knowledge does not exist yet. However, a simple precipitation detection method, which is described in section 3.2, was applied to the data set. In principle, this method can be applied to any Doppler lidar that provides measurements of vertical Doppler velocity and horizontal winds and requires only Doppler lidar; however, it is designed so that it can be easily extended with supplementary information, such as sensible heat flux measurements from a 3-D sonic anemometer.

For this study, we applied the classification method to long-term data sets (over 1 year) to capture a full seasonal cycle of the ABL using instruments at two sites in Europe. The instruments and their operating specifications, together with their locations, are described in section 2. The classification method is presented in section 3, which describes the lidar quantities that are required, together with their associated uncertainties, and the decision tree that is used to assign the source. In section 4, two case studies are highlighted to show how the method performs in both clear-sky and cloudy-topped ABL situations, and the results from the long-term climatological analysis at both sites are discussed.

2. Measurements

2.1. Halo Photonics Streamline Scanning Doppler Lidar

The Halo Photonics Streamline Doppler lidar (Pearson et al., 2009) is a pulsed lidar system with a heterodyne detector operating in the near-infrared spectral region. This instrument has full hemispheric scanning capability and provides range-resolved profiles of backscattering signal and radial Doppler velocity with user-selectable resolution. The instrument parameters during standard operation for the two instruments considered here are given in Table 1. To obtain reliable uncertainty estimates, Manninen et al. (2016) showed that the Halo lidar signal output often requires further processing to account for artifacts in the instrument background signal. This extra processing also has a major impact on the data availability, especially in regions with a low aerosol loading. The extra processing does not affect the Doppler velocities. After the background correction, new measurement uncertainties are derived from the corrected signal (O'Connor et al., 2010; Rye & Hardesty, 1993), which will then propagate through to the products derived from the lidar signal and radial Doppler velocity. Profiles of calibrated attenuated backscatter coefficient (β) are also derived (Westbrook et al., 2010), if the telescope function is known (Hirsikko et al., 2014).

2.2. Site and Data Set Description

To evaluate the ABL classification, Halo lidar measurements from two locations are utilized: Hyytiälä, Finland, and Jülich, Germany. Both locations represent a maritime to continental environment in the high and middle latitudes, respectively. The data set used in this study consists of Halo lidar measurements performed between 1 September 2015 and 15 November 2016 at Hyytiälä and from 1 May 2015 to 31 December 2016 at Jülich.

Hyytiälä hosts the Station for Measuring Ecosystem-Atmosphere Relations-II (Hari & Kulmala, 2005) operated by the University of Helsinki and is located in the southwestern part of Finland (61.845°N, 24.289°E). The site is about 190 km north of Helsinki and 150 km from the shores of the Gulf of Bothnia in the west. The site represents a typical rural boreal forest environment and was established to teach and study forestry in 1910. Together with forest science research, atmospheric measurements have been performed at the station since the 1980s, and the Station for Measuring Ecosystem-Atmosphere Relation-II station has been operational since 1995. The station is embedded within the Aerosols, Clouds and Trace gases Research Infrastructure (ACTRIS), Integrated Carbon Observation System, and Long-Term Ecosystem Research in Europe infrastructures.

The Halo lidar, operated by the Finnish Meteorological Institute, has been operating continuously at the station since 2013, following the operational scanning strategy outlined in Hirsikko et al. (2014). The scanning sequence for this period comprised the following: VAD scan at 30° elevation from horizontal with 23 beams (excluding one blocked beam) every 30 min, three-beam Doppler beam swinging (DBS) scan at 70° elevation every 30 min, and range height indicator scan and custom sector scan every 30 min with slightly varying integration times. When not scanning, the instrument was performing vertical stare measurements with 10-s integration time. For Hyytiälä, only the DBS scans were used for the Halo lidar wind retrievals.

The Jülich ObservatorY for Cloud Evolution (JOYCE) is embedded in the German Research Foundation (DFG) Transregional Collaborative Research Centre Transregio32 Patterns in Soil-Vegetation-Atmosphere Systems—Monitoring, modeling and data assimilation of the Universities of Aachen, Bonn, Cologne, and the Research Centre Jülich. The JOYCE instrumentation aims to observe the variability of atmospheric water cycle variables, helping to understand the interactions between soil, vegetation, and atmosphere through spatially and temporally highly resolved measurements. As a registered DFG Research Infrastructure, JOYCE has recently (beginning of 2016) been funded as a DFG Core Facility in order to professionally manage user access to JOYCE instruments, observation data, and scientific expertise. Internationally, JOYCE is a Cloudnet observatory embedded within the European Horizon2020 Research Infrastructure ACTRIS-2. In March 2016 the European Strategy Forum for Research Infrastructures officially adopted ACTRIS. Most of the instruments (including the Doppler lidar) are located on the roof of the Institute for Energy and Climate Research-Troposphere IEK-8 at the Research Centre Jülich, which is embedded in an agricultural dominated landscape (50.909°N, 6.414°E, 111 masl).

At Jülich, the operational scanning strategy consists of a 75° elevation VAD scan with 36 beams every 15 min. Every 5 min a DBS scan is conducted with the same elevation angle. Since 1 June 2015 an additional VAD scan with only three beams was set up following the DBS scan. Furthermore, a range height indicator scan at 0° azimuth is performed every hour with 5° increments, resulting in 37 beams. For the remainder of the time, vertical stare measurements are carried out with 1-s integration time. For Jülich, only the VAD scans were used for the Halo lidar wind retrievals. To filter atmospheric lidar signal from noise, we have selected a conservative signal-to-noise (SNR) threshold of −20 dB at both sites.

3. Methodology

3.1. Calculation of the Required Quantities From Doppler Lidar Measurements

The ABL classification method requires the following lidar quantities as inputs: attenuated backscatter coefficient, vertical velocity skewness, dissipation rate of turbulent kinetic energy (TKE), vertical profiles of horizontal wind, and vector wind shear. These lidar quantities are derived from the data corrected following Manninen et al. (2016) and generated at the original vertical resolution and selected temporal resolution, unless otherwise mentioned. The choice of temporal resolution depends on the signal strength and data availability, that is, the aerosol loading in the region where the Halo lidar is located; more averaging is required in clean air situations. In addition, it is necessary to ensure that the turbulent length scales imposed by the choice of temporal resolution encompass eddies that remain within the inertial subrange (Frehlich & Cornman, 2002; O'Connor et al., 2010). Hence, for the sites investigated here, 3 min was determined as the temporal

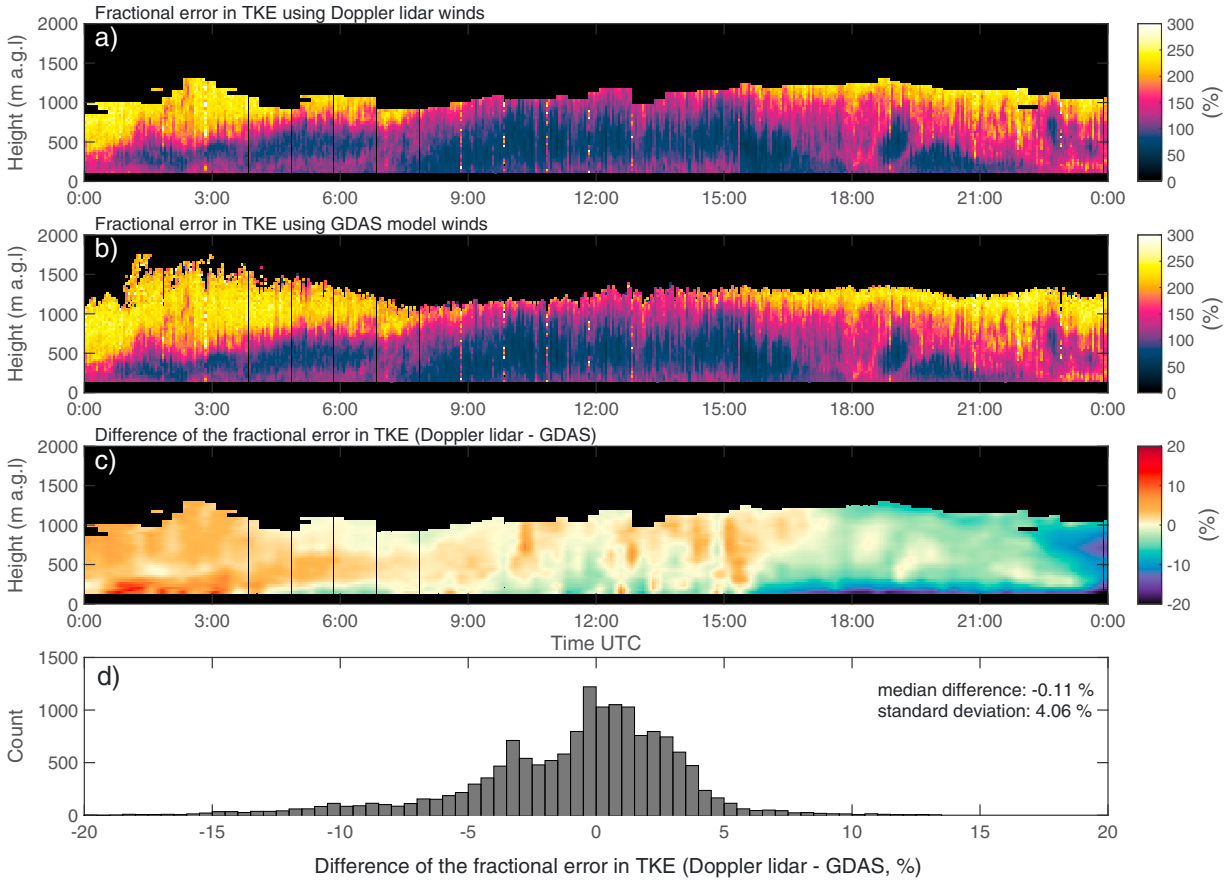

Figure 1. Time-height plots of fractional error in ϵ using (a) Doppler lidar winds and (b) GDAS model winds calculated from measurements on 9 March 2016 at Jülich, Germany. (c) Time-height plot and (d) histogram of the difference in the two fractional errors (Doppler lidar-GDAS). GDAS = Global Data Assimilation System; TKE = turbulent kinetic energy.

resolution limit for generating the ABL classification. Vertical velocity skewness requires a longer time window (e.g., Harvey et al., 2013; Hogan et al., 2009), which is further discussed below.

The height of the aerosol layer, in terms of the Halo lidar measurements, is calculated from the averaged attenuated backscatter coefficients (β). The height is utilized to limit the calculations to the height ranges with sufficient atmospheric signal. Clouds are detected from the β values by selecting a threshold from the literature: 10^{-5} $m^{-1}\cdot sr^{-1}$ (e.g., Harvey et al., 2013; Hogan et al., 2009; Westbrook et al., 2010). Ideally, the cloud detection scheme should include objective cloud-precipitation discrimination.

The uncertainty in attenuated backscatter coefficient σ_β is calculated by

$$\sigma_\beta = \frac{1}{\sqrt{n_p}}\left(1+\left(\frac{1}{|\mathrm{SNR}|}\right)\right), \tag{1}$$

where n_p is the number of pulses per ray and SNR is the signal-to-noise ratio. Since the β value at cloud base is at least 2 orders of magnitude above aerosol β values, and usually have high SNR, we consider that σ_β has little impact on the simple threshold-based cloud detection method.

The vertical velocity variance and skewness are calculated from the vertically pointing radial Doppler velocities by using a method presented by Rimoldini (2014), which provides higher-order moments unbiased by random uncertainties or sample size. The vertical velocity skewness is used to diagnose whether the turbulence is cloud driven, as discussed in section 3.2.2. Uncertainties of velocity variance and skewness were estimated by using bootstrapping technique (e.g., Kleiner et al., 2014). To capture reliable skewness of vertical air motion in the ABL, a 60-min time window was determined to be suitable. Skewness calculated with

the 60-min window is then subsampled to 3 min with linear interpolation to match the temporal resolution of other lidar quantities. Skewness is highly noisy quantity, and thus, in the results presented here, median filtering is applied using a window size of 10 consecutive 3-min profiles and 3 range gates.

In order to associate a source of the mixing process, the most important part of the classification is the identification of the turbulent regions of the ABL. Hogan et al. (2009) discussed that a combination of vertical velocity skewness and variance (σ_v^2) can be used to detect turbulence. In this study, the presence of turbulent mixing is diagnosed from the dissipation rate of TKE, which is calculated from vertically pointing data using the method presented by O'Connor et al. (2010):

$$\epsilon = 2\pi \left(\frac{2}{3a}\right)^{3/2} \sigma_{\bar{w}}^3 \left(L^{2/3} - L_1^{2/3}\right)^{-3/2}, \tag{2}$$

where the $a = 0.55$ is the Kolmogorov constant, $\sigma_{\bar{w}}$ is the standard deviation of the mean radial velocity of a selected time averaging window (O'Connor et al., 2005), L is the length scale of the largest eddies that pass completely through the lidar beam during the averaging window, and L_1 describes the length scale of the scattering volume dimension per single sample in the averaging window. It is important to note that, if present, the impact of wave motions to the observed $\sigma_{\bar{w}}$ and henceforth to the ϵ should be taken into account because the wave motions do not cause turbulent mixing (Bonin et al., 2018).

The method also provides an uncertainty estimate for ϵ, described in terms of fractional error, $\Delta\epsilon/\epsilon$, where $\Delta\epsilon$ is the absolute error in TKE dissipation rate (for further details, see O'Connor et al., 2010). Horizontal winds are required to estimate the length scales L and L_1, and these may be provided by the instrument itself, if scanning capable, or by supplementary sources such as radiosonde, wind profiler, or weather forecast models (O'Connor et al., 2010). Low SNR or highly turbulent conditions can impact the Doppler lidar wind retrievals (Newsom et al., 2017; Päschke et al., 2015), in which case, when Halo lidar horizontal winds are not available, horizontal winds provided by, for example, the Global Data Assimilation System, GDAS (GDAS, 2016) can be used instead.

To investigate how the uncertainty in ϵ estimate change when model winds are used instead of winds retrieved with Doppler lidar, we calculated ϵ using (2) with both wind data sets and compared the resulting fractional errors in ϵ. Figure 1 shows an example day from 9 March 2016, Jülich, Germany, where Halo lidar winds could be retrieved throughout the ABL. The median difference in fractional error in ϵ was 0.11% with standard deviation of 4.1%. Given that a typical threshold value for reliable ϵ estimates can be as high as 300%, as suggested by O'Connor et al. (2010), the additional uncertainty arising from using GDAS model winds is considered to be insignificant. However, in the results presented in this paper we have used only the Halo lidar winds.

Wind shear, which is also a source of turbulent mixing, can be derived from the Doppler lidar retrievals of horizontal wind. The vector wind shear is given by, for example, ICAO (2005):

$$\text{vector wind shear} = \frac{\left(\Delta u^2 + \Delta v^2\right)^{1/2}}{\Delta z}, \tag{3}$$

where the vector difference of the u and v wind components is divided by the height difference Δz between the two altitudes over which the wind shear is calculated. Here the vector wind shear is calculated over three range gates ($\Delta z = 90$ m). The uncertainty in vector wind shear is obtained by propagating the uncertainty in the winds. In good conditions, the uncertainty in horizontal wind is of the order 0.2 m/s for VAD scans, but inhomogeneous flow in strongly turbulent mixing layers can increase the uncertainty significantly (Päschke et al., 2015). Thus, we assume that, when present, convective mixing is the dominant cause of turbulence within the ABL and neglects the influence of vector wind shear. Wind shear is not calculated when Doppler lidar winds are not available.

For additional information, the low-level jet (LLJ) detection algorithm presented by Tuononen et al. (2017) is applied. LLJs have been shown to cause shear-driven turbulence above and below the jet nose, especially in the nighttime ABL (Banta et al., 2006; Cuxart & Jiménez, 2007) and also during daytime in coastal locations (Tuononen et al., 2017). In the results presented here, only the presence and the height of the detected LLJs are shown, but LLJs are not explicitly diagnosed as the turbulent source, as automated attribution is still under evaluation.

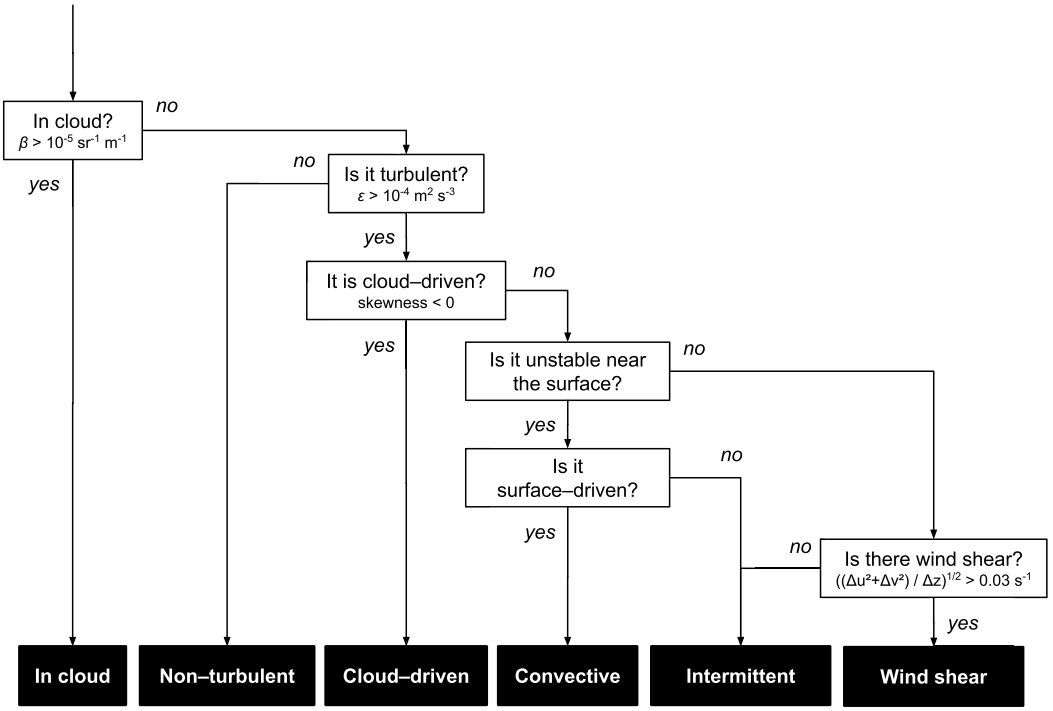

Figure 2. Schematic of the atmospheric boundary layer turbulent mixing source decision tree.

3.2. Generating the ABL Classification Product

The main product of the method presented in this paper is a classification bit field, in which each bit contains the relevant information obtained from each individual quantity required for the boundary layer classification. The two masks, generated using the decision tree logic, are derived from the bit field. This approach allows straightforward implementation of future developments, such as improved methods and supplementary information (e.g., surface stability), through which new bits can be added to the bit field, without changing the current logic. The decision tree logic can be modified without modifying the bits, and more classes can be added by including the new bits when deriving masks from the bit field. The bit field can be represented by two fields, one identifying the presence of turbulent mixing and whether it is associated with clouds, the surface, or neither (section 3.2.1) and one presenting the diagnosed dominant source of mixing (section 3.2.2). These fields are generated at the same time-height resolution as the input lidar quantities. The classification product classes are denoted in italics.

Precipitation cases are identified profile by profile from the vertical velocity data by using the assumption that all precipitation has a fall velocity greater than 1 m/s. Since turbulent motions can also exceed 1 m/s, a pixel-by-pixel approach will not suffice. However, a mean negative Doppler velocity averaged over a larger time and vertical window is also not a sufficient discriminator, since large turbulent eddies can also result in a mean negative Doppler velocity at the time and spatial scales that would seem suitable for detecting precipitation. Hence, we use the additional criterion that 95% of the Doppler velocities within the averaging window must also be < -1 m/s; the entire profile within which any pixel meets these criteria is then diagnosed as containing precipitation. An averaging window of 3×7 pixels (equivalent to 9 min and 210 m) was applied to the 3-min averaged profiles; since precipitation is more coherent in the vertical dimension, enlarging the window in the vertical direction provides more values from which to compute the 95th percentile and is a compromise between obtaining a robust result and retaining the temporal resolution necessary to capture some precipitation features. This precipitation diagnostic may not be suitable in locations where there is significant large-scale vertical motion arising from orographic features or strong convection. At the two locations in this study, the precipitation diagnostic removed about 1% of the profiles at Hyytiälä and about 2% at Jülich.

3.2.1. Surface-Driven Versus Cloud-Driven Turbulent Mixing

The presence of turbulence is obtained from ϵ using a threshold-based approach. Previous studies suggest $\epsilon > 10^{-4}$ m^2/s^3 as a suitable threshold value (e.g., Borque et al., 2016; O'Connor et al., 2010; Vakkari et al., 2015).

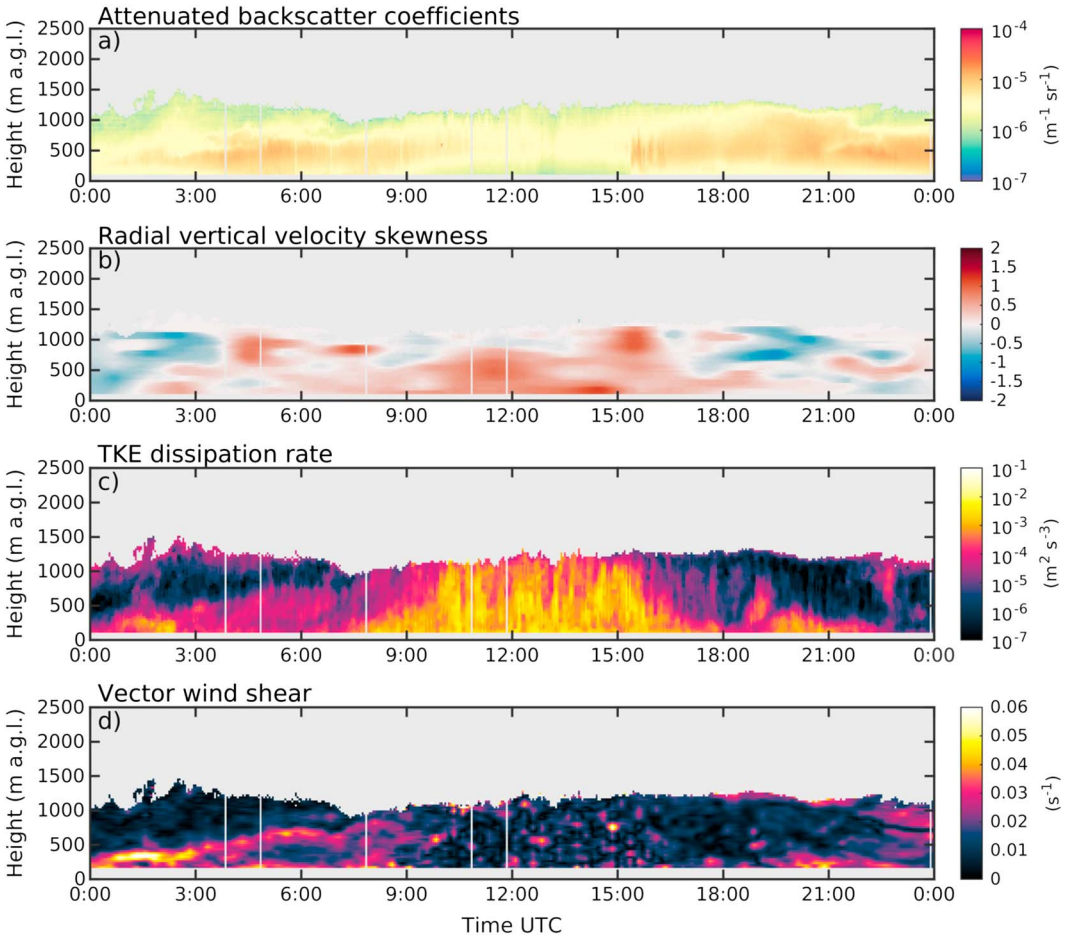

Figure 3. Time-height plots of (a) attenuated backscatter coefficient, β, (b) vertical velocity skewness, (c) TKE dissipation rate, ϵ, and (d) vector wind shear, calculated from Doppler lidar measurements on 9 March 2016 at Jülich, Germany. Solar noon is about 11:45 UTC. TKE = turbulent kinetic energy.

We selected $\epsilon > 10^{-5}$ m^2/s^3 as our threshold for detecting turbulent mixing and a threshold of $\epsilon > 10^{-4}$ m^2/s^3 for detecting surface-connected mixing, as discussed below. Pixels above the $\epsilon > 10^{-5}$ m^2/s^3 threshold are determined to be turbulent and below the threshold as *nonturbulent*. The presence of cloud in a profile is also determined using a threshold value, $\beta > 10^{-5}$ m^{-1}·sr^{-1} being labeled as *in cloud*.

When the ABL is topped by stratocumulus clouds, cloud-top radiative cooling can be the dominant driver for turbulent mixing within the ABL (Wood, 2012), which resembles the inverse of surface-driven turbulence (Hogan et al., 2009) and can be recognized from the vertical velocity skewness. In order to determine whether turbulent mixing is associated with a cloud layer, labeled *cloud driven*, the cloud base height is first obtained and then a top-down approach is used to find all consecutive range gates below the cloud with $\epsilon > 10^{-5}$ m^2/s^3 and containing negative vertical velocity skewness. Similarly, *surface connected* is resolved with a bottom-up approach by searching the profile upward until the first range gate where $\epsilon < 10^{-4}$ m^2/s^3 is found, starting at the lowest reliable range gate of the Halo lidar (105 m). Any remaining range gates where $\epsilon > 10^{-5}$ m^2/s^3 are labeled as *unconnected*. In principle, the regions labeled surface connected comprise the mixing layer, from which the mixing layer height can be produced, a valuable parameter for many applications. Cases where the surface-connected and cloud-driven turbulence are coupled, special care should be taken in determining the height of the mixing layer since ascending and descending plumes have been observed to pass through the interface between positive and negative skewness layers indicating surface-connected and cloud-driven layers, respectively (Hogan et al., 2009).

3.2.2. Identifying the Turbulent Mixing Source

The source of turbulent mixing is derived using decision tree-based logic, as presented in Figure 2, which requires an additional input describing the atmospheric thermodynamic stability close to the surface.

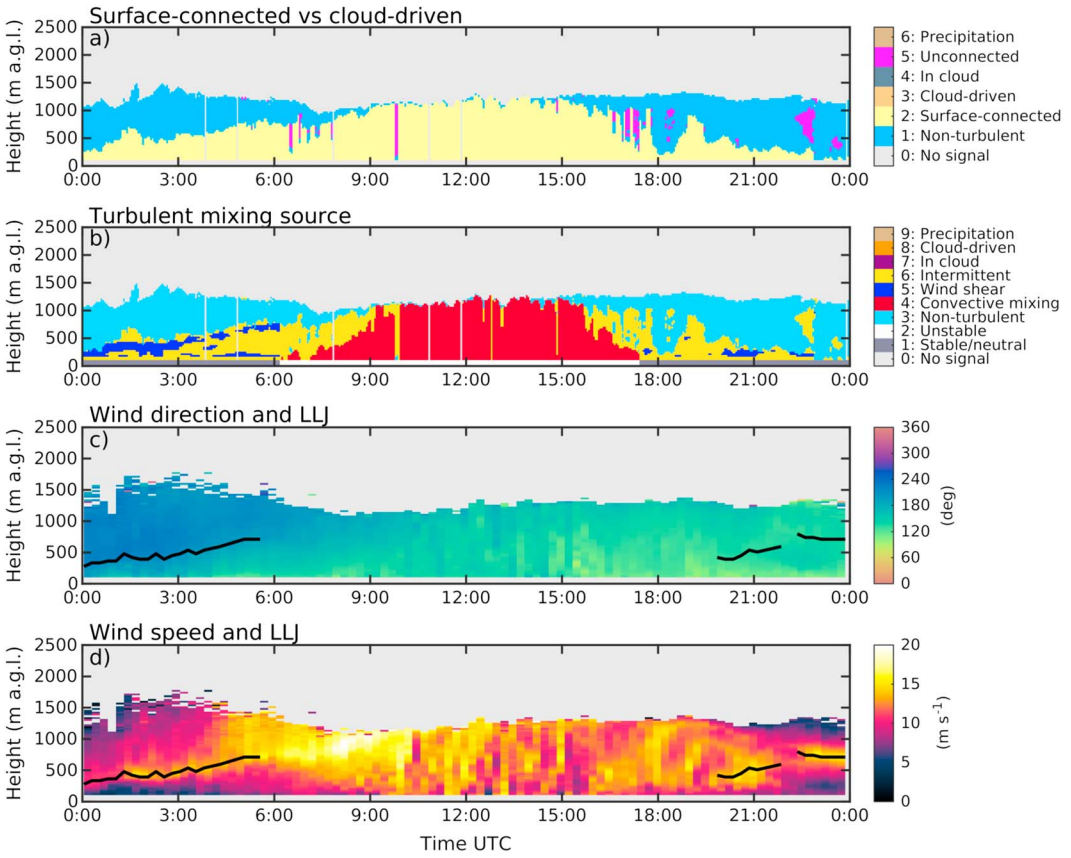

Figure 4. Time-height plots of atmospheric boundary layer classification showing (a) connection with the surface (i.e., surface driven versus cloud driven) and (b) the turbulent mixing source, together with time-height plots of (c) wind direction and (d) wind speed on 9 March 2016 at Jülich, Germany. The black lines on the two lower panels show LLJ altitude identified using the method presented by Tuononen et al. (2017). LLJ = low-level jet.

First, pixels are identified as being in cloud or not. Then, turbulent pixels are separated from nonturbulent and cloud-driven pixels are identified. Other turbulent pixels are then classified depending on the atmospheric stability close to the surface, whether they are in contact with the surface, and whether there is wind shear present.

In the absence of ancillary measurements, it is assumed that the daytime ABL is unstable, and the nighttime ABL is neutral or stably stratified (e.g., Garratt, 1994; Oke, 1992), with sunrise and sunset calculated using the method described in Ibrahim and Afshin (2008). In unstable situations, *convective* mixing is assumed to be the dominant source of turbulence for pixels labeled surface connected. It is important to note that the ABL does not become unstable immediately after sunrise but that it takes some time, the length of which depends, for example, on solar angle, cloud cover, and surface characteristics (Ketzler, 2014).

In stable or neutral conditions, any turbulence in the presence of significant wind shear, defined as $> 0.03\ s^{-1}$, is assigned the class *wind shear*, which may include surface-connected and unconnected pixels (but not cloud driven), and is often seen in the presence of a LLJ as in the case study discussed in section 4.1. This class is not assigned in unstable situations as it is assumed that any mechanically driven turbulence is dominated by thermally driven turbulence.

For all remaining unassigned pixels, turbulence is assumed to arise from decaying convective eddies after sunset or from other intermittent sources (Lothon et al., 2014) and labeled as *intermittent*.

4. Results and Discussion

We first present two case studies, a clear-sky day from Jülich and a cloud-topped ABL from Hyytiälä, to illustrate the detailed performance of the classification scheme on a daily basis. The ABL classification scheme is

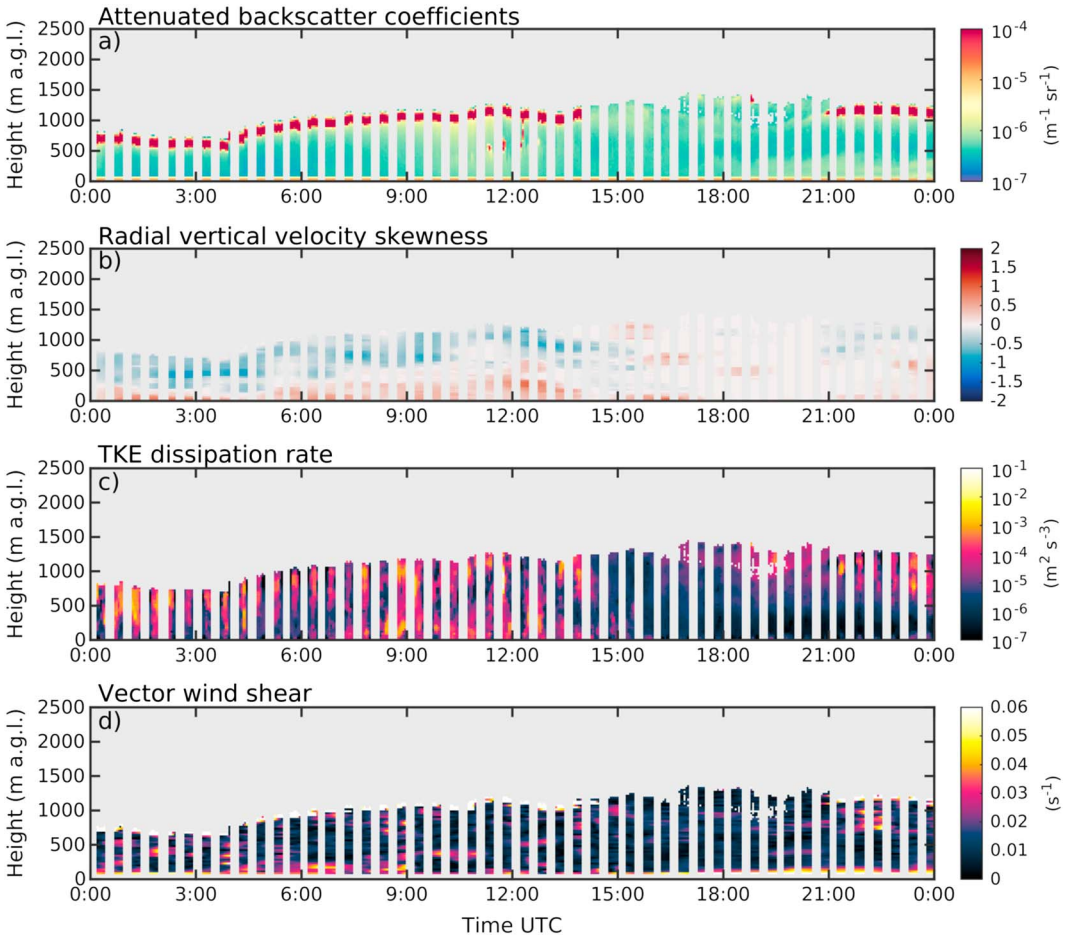

Figure 5. Time-height plots of (a) attenuated backscatter coefficient, β, (b) vertical velocity skewness, (c) TKE dissipation rate, ϵ, and (d) vector wind shear, calculated from Doppler lidar measurements on 22 September 2016 at Hyytiälä, Finland. Vertical gray lines indicate periods when the Doppler lidar was scanning. Solar noon is about 10:15 UTC. TKE = turbulent kinetic energy.

then applied to more than 1 year of data from both sites to display how the classification scheme is used to investigate the relative proportion of surface-driven, cloud-driven, and other turbulent sources, their diurnal cycle, and their seasonal variation.

4.1. Clear-Sky Case Study

Figure 3 displays lidar quantities calculated from the Halo lidar data for a clear-sky day in Jülich, Germany. The development of the ABL structure is typical for a clear-sky day between spring and early autumn in a midlatitude and semiurban environment. Sunrise is at 06:08 UTC, and a layer with high TKE dissipation rate values ($\epsilon > 10^{-3}$ m^2/s^3) and generally positive skewness values can be seen growing to reach about 1,200 m by 10:00 UTC, indicative of surface-driven convective mixing. This layer then begins reducing in altitude after 16:00 as the turbulent mixing associated with surface heating weakens, as expected with sunset at 17:24 UTC. The ABL classification product displayed in Figure 4, diagnosed using the decision tree (Figure 2), produces the same result, *surface-connected* mixing with a convective source during the daytime.

However, there are other turbulent features present in the ABL. Between 00:00 and 09:00 UTC there is significant turbulent mixing at altitudes up to 500 m or more, the upper boundary of which coincides with a strong gradient in the attenuated backscatter field. This early morning turbulent mixing correlates well with an elevated layer of strong vector wind shear (> 0.03 s^{-1}) as does another elevated turbulent layer after sunset between 17:30 and 22:30 UTC. Applying the LLJ algorithm to the horizontal wind profiles, displayed in Figure 4, shows that LLJs are present at these times and at appropriate altitudes, since the strongest wind shear associated with LLJs is usually below the jet maximum. There is also strong near-surface shear cou-

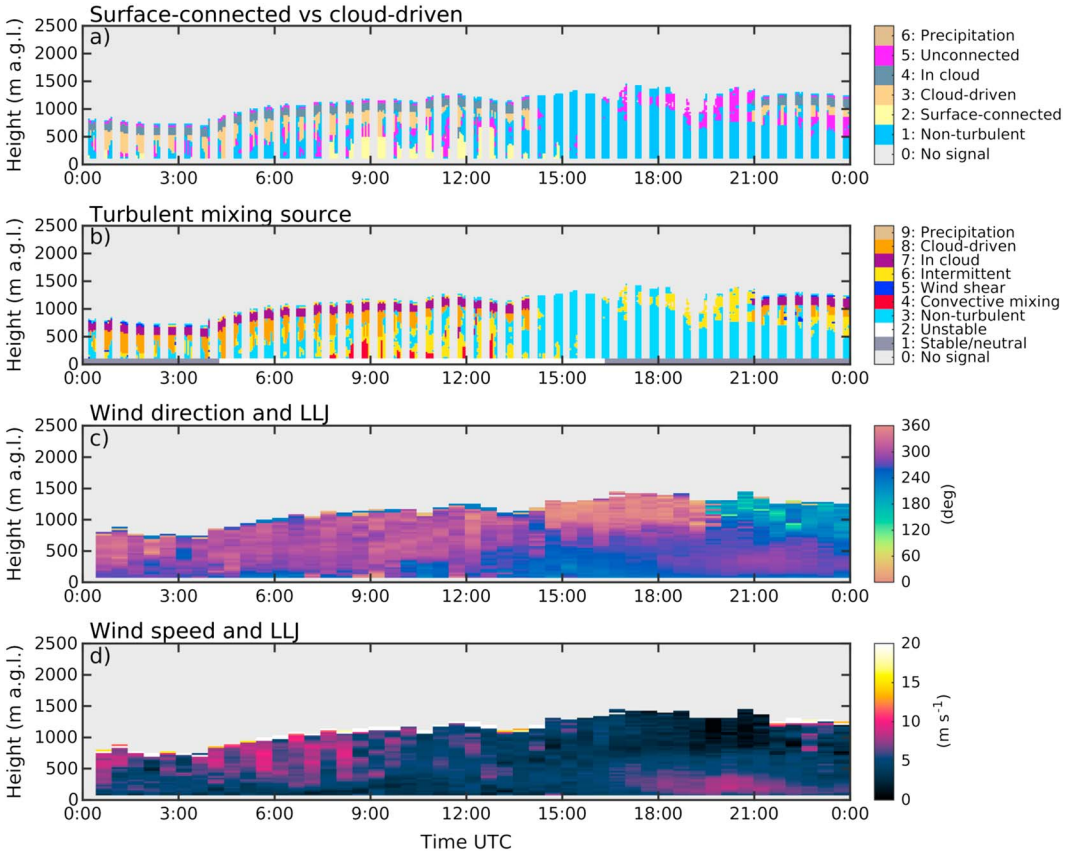

Figure 6. Time-height plots of ABL classification showing (a) connection with the surface (i.e., surface driven versus cloud driven) and (b) the turbulent mixing source, together with time-height plots of (c) wind direction and (d) wind speed on 22 September 2016 at Hyytiälä, Finland. Vertical gray lines in (a) and (b) indicate periods when the Doppler lidar was scanning. LLJ = low-level jet.

pled with turbulence detected between 00:00 and 4:00 UTC and between 18:00 and 24:00 UTC, presumably a result of the surface friction. These features are also captured in the classification product as wind shear and may be surface connected or unconnected. Turbulent features without an objectively determined source are labeled as intermittent. In this pixel-by-pixel approach we assume that convective mixing dominates any wind shear, since convection also manifests apparent wind shear at the 3-min resolution used here (due to updrafts and downdrafts being advected over the site). Outside convective regions, pixels classified as intermittent might also be a result of wind shear but not directly affected by wind shear. For interpreting wind shear-affected regions, temporal and spatial consistency of the classification should be considered, and the wind shear threshold sensitivity tests should be carried out at several sites.

Note that there are weak features that could be interpreted as decaying turbulence in Figure 3c, such as after 16:00 UTC up to 1 km, but since $\epsilon < 10^{-4}$ m^2/s^3 the decaying turbulence is labeled accordingly as nonturbulent in Figures 4a and 4b. This is a consequence of the relatively high fractional errors in dissipation rate for low ϵ values.

4.2. Cloud-Topped Case Study

Figure 5 displays the same lidar quantities as in Figure 3 calculated from the Halo lidar data for a nonprecipitating stratocumulus cloud-topped case in Hyytiälä, Finland. Exhibiting high attenuated backscatter ($\beta > 10^{-4}$ m$^{-1}\cdot$sr^{-1}), the stratocumulus cloud layer is clearly visible in Figure 5a at altitudes ranging from 500 m between 00:00 and 04:00 UTC and rising to about 1,000 m by 06:00 UTC. The stratocumulus layer persists until 14:00UTC and then reappears in the evening after 21:00 UTC, with clear skies in between. A deep layer of high dissipation rate ($\epsilon > 10^{-4}$ m^2/s^3) and negative skewness values is associated with the cloud layer and is not present during the clear-sky period in the afternoon. In the morning, between 00:00 and 05:00 UTC, this layer

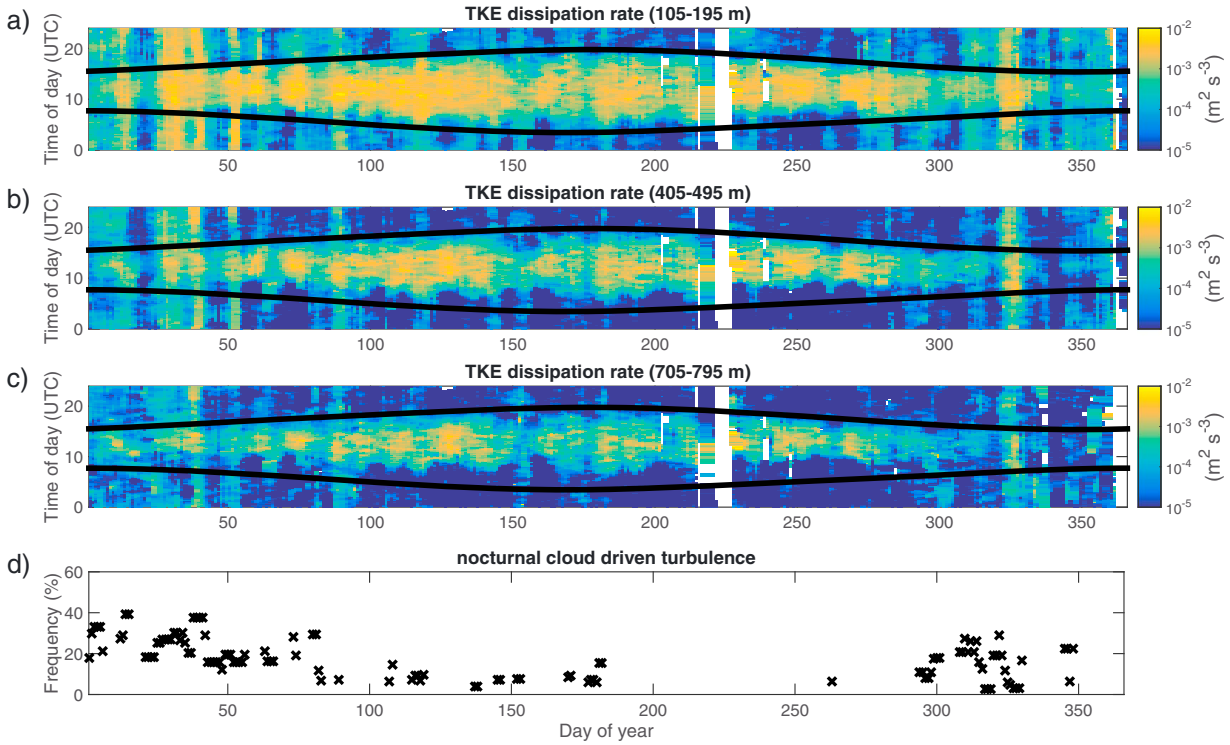

Figure 7. Time-of-day versus day-of-year plot of TKE dissipation rate ϵ values from Jülich, Germany, averaged over altitude ranges: (a) 105–195 m above ground level (agl), (b) 405–495 m agl, and (c) 705–795 m agl. Black lines in (a)–(c) show sunrise and sunset. Panel (d) presents the frequency of occurrence of nocturnal cloud-driven turbulence. A moving median filter of 5 days and 30 min has been applied to the data. Data period is between 1 May 2015 and 31 December 2016. TKE = turbulent kinetic energy.

can be seen to reach from cloud base down to about 200-m altitude between 00:00 and 05:00 UTC (Figures 5b and 5c), below which exists a layer with positive skewness values, indicating that although cloud-driven turbulent mixing dominates most of the ABL depth, it is not able to mix through to the surface. Once the cloud layer is not present, after 14:00 UTC, the turbulent mixing associated with the cloud also disappears rapidly, with the skewness values switching from negative to positive in the absence of any turbulent source. Negative skewness values return in the evening at 21:00 UTC and at 1,000 m when the stratocumulus layer reappears, with a turbulent layer growing below cloud base.

After sunrise at 04:24 UTC, a turbulent layer with positive skewness values indicating surface-driven mixing grows from the surface to reach 800 m by 14:00 UTC, before decaying again toward sunset at 16:29 UTC. Although relatively high dissipation rate values are present throughout much of the ABL between 00:00 and 15:00 UTC, strong gradients in vertical velocity skewness and dissipation rate suggest that there are two turbulent layers and little mixing across the boundary between them. These features are captured in the ABL classification product in Figure 6, which shows separate regions of mixing: one connected to clouds (cloud driven), one connected to the surface (surface connected) and associated with convective mixing. Cumulus clouds at 500 m in altitude are present around 12:00 UTC, and correctly identified by the classification as being surface connected, due to the positive skewness values and connection of the turbulent layer to the surface. There are also regions labeled intermittent or wind shear where the turbulent ABL has been identified, but, due to alternating positive and negative patterns observed in the vertical velocity skewness (e.g., between 22:00 and 23:00 UTC), the objective nature of the classification scheme does not issue a definitive association with the surface or cloud layer.

Hence, the classification scheme is able to distinguish between coupled and decoupled clouds, identify the layer of mixing associated with clouds and whether it dominates any surface-driven mixing, and aid in determining whether cumulus clouds formed underneath a stratocumulus cloud layer act to couple the stratocumulus layer to the surface (Krueger et al., 1995; Wood, 2012).

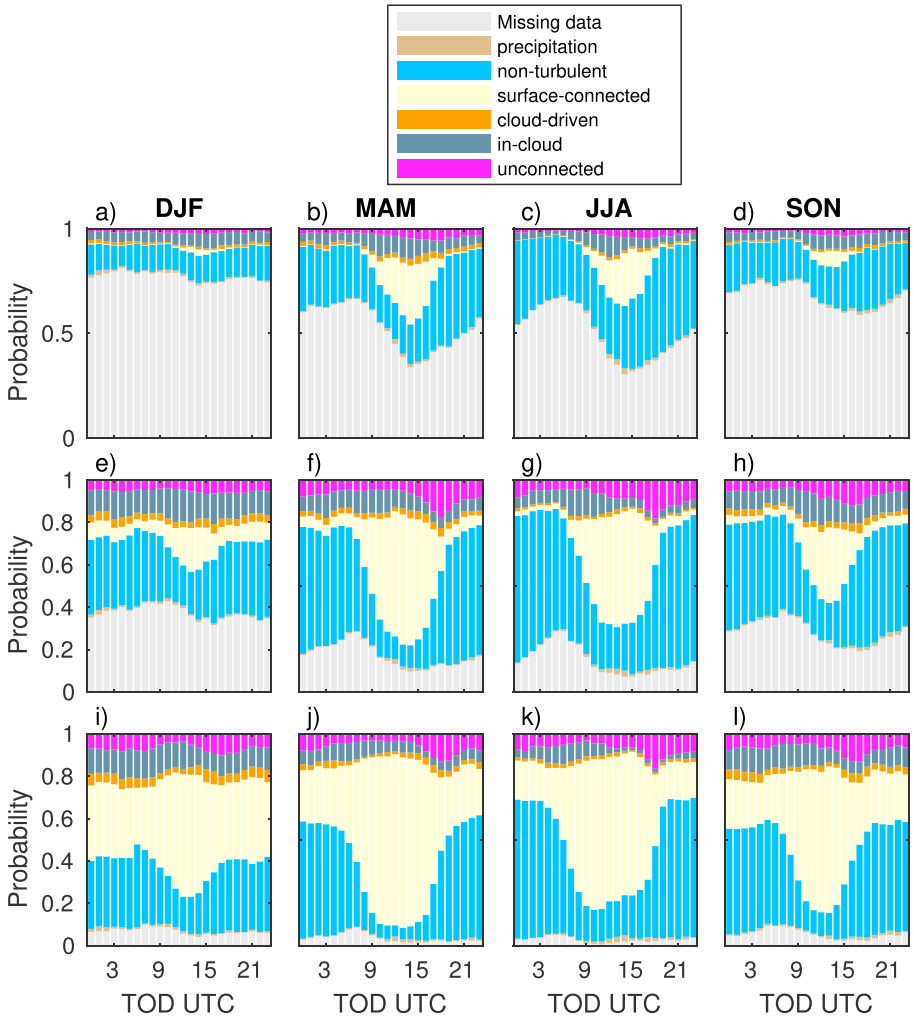

Figure 8. Seasonal average diurnal cycle of the probability of turbulence over Jülich, Germany, to be associated with the surface, cloud, or neither, calculated for three different height ranges: (a–d) 1,065–1,515 m above ground level (agl), (e–h) 585–1,035 m agl, and (i–l) 105–555 m agl. Measurement period covers 1 May 2015 to 31 December 2016. DJF = December–February; MAM = March–May; JJA = June–August; SON = September-November; TOD = time of day; UTC = universal time coordinated.

4.3. Climatological Analysis

Figure 7 displays TKE dissipation rate with respect to the time of day and day of year from Jülich, Germany. There is a clear diurnal and seasonal cycles, and the presence of strong dissipation rate generally lies between sunrise and sunset. The time lag between sunrise and the onset of turbulence increases with altitude, and, above 400 m, the atmosphere is typically calm before sunrise and after sunset. However, there are also periods where there is no diurnal cycle, visible in the plots as vertical bands of high dissipation rate, and these are connected to days where turbulence in the ABL is mainly driven by clouds (Figure 7d, which shows the percentage of nighttime profiles per day with at least one pixel of cloud-driven turbulence).

To investigate the seasonal changes in the diurnal cycle of the mixing in the ABL, the data sets from both sites were divided into four seasons: winter (December–February), spring (March–May), summer (June–August), and autumn (September–November). The seasonal changes in the diurnal cycle of the probability for the turbulence to be connected with the surface, or not, are shown for Jülich in Figure 8 and for Hyytiälä in Figure 9. In both figures, the statistics were calculated over three different altitude ranges, selected so that the ABL development at both sites could be compared despite the differences in their average daily maximum ABL height. The amount of missing data increases with altitude at both sites, as expected since SNR reduces with range, and signal is usually confined to the ABL. After background correction, the same conservative SNR

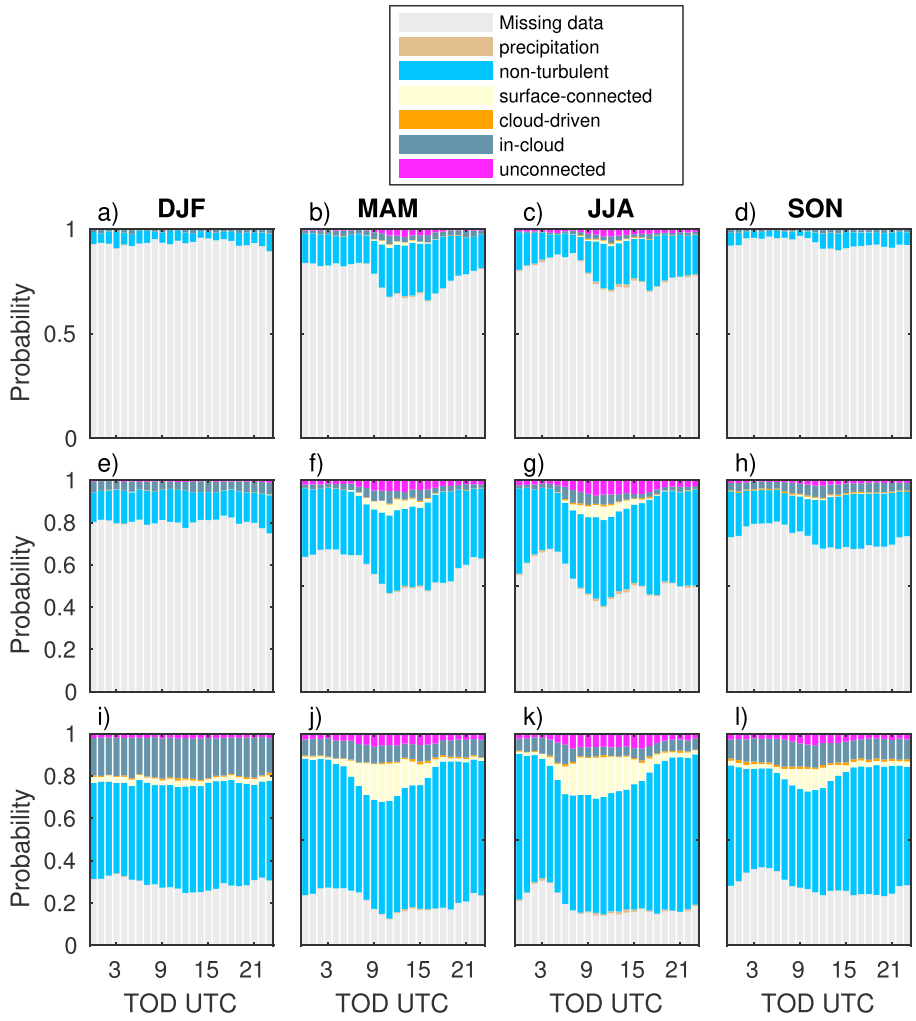

Figure 9. Seasonal average diurnal cycle of the probability of turbulence over Hyytiälä, Finland, to be associated with the surface, cloud, or neither, calculated for three different height ranges: (a–d) 1,065–1,515 m above ground level (agl), (e–h) 585–1,035 m agl, and (i–l) 105–555 m agl. Measurement period covers 1 September 2015 to 15 November 2016. DJF = December–February; MAM = March–May; JJA = June–August; SON = September-November; TOD = time of day; UTC = universal time coordinated.

threshold of −20 dB (0.01) was chosen for both sites; thus, the large difference in the amount of missing data between the sites portrays how much the aerosol loading impacts data availability. Jülich exhibits a clear seasonal and diurnal dependence in data availability for the highest altitude range, with most missing data during winter (> 70%) and least during summer afternoons (< 40%), directly responding to the large seasonal variation in ABL depth in the midlatitudes. At Hyytiälä, a high-latitude site, the amount of missing data is consistently above 70% for the highest altitude range in all seasons, and it is the medium altitude range that resembles more closely the upper altitude range at Jülich. The ABL does reach 1,500 m in summer over Hyytiälä, but the corresponding dilution of the already low aerosol loading through the deeper ABL often results in SNR that is too weak to generate reliable lidar quantities for classification. The ABL height in winter at Hyytiälä rarely reaches 500 m, hence the very low data availability above 500 m.

During spring (Figures 8b, 8f, and 8j and 9b, 9f, and 9j) and summer (Figures 8c, 8g, and 8k and 9c, 9g, and 9k), both sites display a clear diurnal cycle in the probability of turbulence connected with the surface: high during the day (Jülich > 80% and Hyytiälä > 30%) and low during nighttime (Jülich < 20% and Hyytiälä < 10%). A similar but weaker diurnal cycle is evident at both sites during autumn (Figures 8l and 9l): high during the day (Jülich > 60% and Hyytiälä > 20%) and low during nighttime (Jülich < 20% and Hyytiälä < 10%).

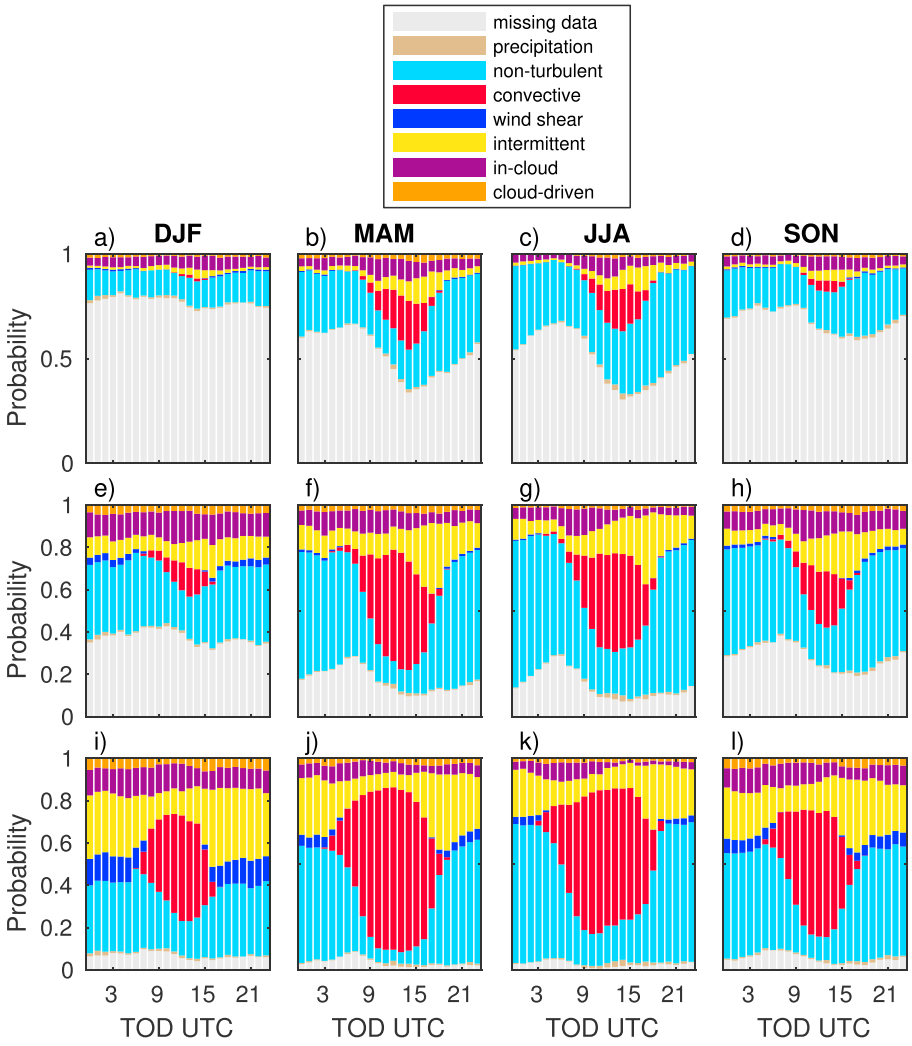

Figure 10. Seasonal average diurnal cycle of the probability for each identified source causing mixing in the atmospheric boundary layer over Jülich, Germany, calculated for three different height ranges: (a–d) 1,065–1,515 m above ground level (agl), (e–h) 585–1,035 m agl, and (i–l) 105–555 m agl. Measurement period covers 1 May 2015 to 31 December 2016. DJF = December–February; MAM = March–May; JJA = June–August; SON = September-November; TOD = time of day; UTC = universal time coordinated.

The probability for unconnected turbulence is highest during spring and summer, especially in the middle height range of 585–1,035 m above ground level (agl) and also noticeable at other height ranges at Jülich (Figures 8f and 8g) and also displays a weak diurnal cycle. This cycle is most obvious during summer, where the probability of unconnected turbulence increases during the afternoon around 18:00 UTC at Jülich. Hence, it is associated with the decay of what was the surface-driven convective mixing layer after the residual layer decouples from the surface. Diurnal cycle in the unconnected turbulence is weaker at Hyytiälä and only noticeable at the middle height range (Figures 9f and 9g).

Figures 8 and 9 also show that clouds influence mixing in the ABL at both sites. There is a strong seasonal variation in cloud presence at each altitude range, with Hyytiälä having probabilities above 30% in winter and 10% in summer at the lowest altitude range, but the diurnal variation is not so pronounced, especially in winter, spring, and autumn. In summer, there are fewer clouds during the day (Hyytiälä) or in late afternoon (Jülich) but these figures do not necessarily capture the full cloud cover, since there may be clouds associated with the ABL above the altitude range maximum (1,515 m agl) selected here.

In Figures 10 and 11 we investigate the seasonal and diurnal cycles in the source of mixing that has been assigned. These figures clearly show the strong diurnal variation in surface-connected convective mixing at

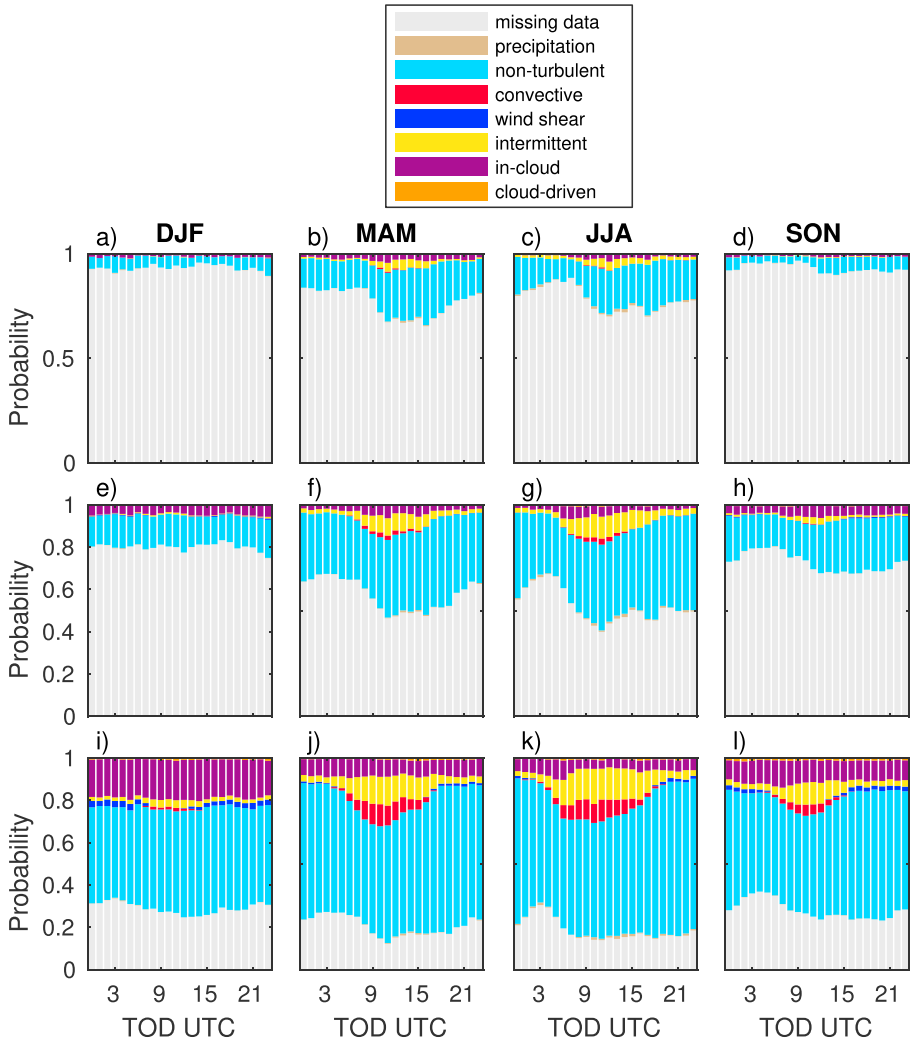

Figure 11. Seasonal average diurnal cycle of the probability for each identified source causing mixing in the atmospheric boundary layer over Hyytiälä, Finland, calculated for three different height ranges: (a–d) 1,065–1,515 m agl, (e–h) 585–1,035 m agl, and (i–l) 105–555 m agl. Measurement period covers 1 September 2015 to 15 November 2016. Measurement period covers 1 May 2015 to 31 December 2016. DJF = December–February; MAM = March–May; JJA = June–August; SON = September-November; TOD = time of day; UTC = universal time coordinated.

both sites and also show the variation in the convective boundary layer with the season. At Jülich, convective mixing at low altitudes clearly dominates ABL mixing during spring, summer, and autumn daytime, but the relative dominance decreases with increasing altitude. Figure 10 shows that convective mixing rarely reaches above 1 km in autumn and winter. A similar picture is seen in Hyytiälä (Figure 11), except that surface-driven convective mixing only dominates during spring and summer at low altitudes and rarely reaches 600 m during autumn and never in winter.

At both sites there is a significant fraction of the time where turbulent mixing is present in the lowest altitude range at night, close 20% in summer but exceeding 40% in winter. At Hyytiälä, most of the nighttime turbulence is associated with cloud, whereas at Jülich, there are larger contributions from other sources. Both sites show a clear seasonal variation in nighttime mixing associated with wind shear at low altitudes, with more observed during autumn and winter than during spring and summer. At Jülich, wind shear is diagnosed almost 10% of the time at night during winter, together with a much higher fraction of intermittent turbulence, where a source of mixing was not assigned. It is thought that LLJs may be partially responsible for the high occurrence of mixing close to the surface at night in Jülich.

Similar seasonal and diurnal variabilities in the extent of the mixed-layer were found over Jülich by Schween et al. (2014) and over Trainou in France by Pal et al. (2015), including the day-to-day variability. However, they limited their studies to identifying the mixed-layer height.

5. Conclusions

In this study, we present a method for objectively classifying turbulent mixing within the ABL using Doppler lidar. The method identifies the presence of turbulence and then assigns a turbulent source by combining several lidar quantities: attenuated backscatter coefficient, vertical velocity skewness, TKE dissipation rate, and vector wind shear. The range of complexity exhibited by ABL mixing was simplified by concentrating on only a finite number of classes and situations that can be identified reliably from Doppler lidar measurements. For instance, we have defined that convective mixing is surface-driven only, even though there are situations where elevated convection can also occur (Geerts et al., 2017).

The method operates in all weather conditions, both clear-sky and cloud-topped, and can provide an ABL classification at high temporal (3 min) and vertical resolution (30 m). The method was applied to extended data sets from Doppler lidar measurements at two locations in different environments, Jülich, Germany, and Hyytiälä, Finland, and was shown to be capable of classifying complex ABL structures. Some limitations were identified, such as insufficient instrument sensitivity during periods with very low aerosol concentrations and difficulties in precipitation discrimination. Synergy with additional instruments would improve this classification method, through providing robust precipitation discrimination or determining the atmospheric thermodynamic stability (e.g., utilizing a vertical temperature gradient from a meteorological tower or the sensible heat flux from eddy covariance measurements). However, this method was designed to operate on Doppler lidar measurements alone since colocated supplementary measurements are not always available at every Doppler lidar site.

Statistical analysis of the data sets measured at Hyytiälä and Jülich showed a very clear seasonal variation in the diurnal cycle for both the probability of turbulence to be associated with the surface, or not, and in the probability of the turbulent mixing source. For these sites, spring, summer, and autumn seasons display a clear diurnal cycle, with surface-driven convection a dominant source of mixing within the ABL during the day, as expected. In winter, as a consequence of their respective latitudes, the diurnal cycle is much weaker at Jülich and almost nonexistent at Hyytiälä. However, there are significant contributions from other sources, with cloud-driven mixing being observed even within the first 500 m from the surface. Also evident is the considerable amount of nocturnal mixing within the lowest 500 m at both sites, especially during the winter. The presence of a LLJ was often detected when sources of nocturnal mixing were diagnosed as wind shear. LLJs are clearly an important source of mixing, promoting mixing especially below the jet.

The classification scheme and the climatology extracted from the classification provide insight into the processes responsible for mixing within the ABL, how variable in space and time these can be, and how they vary with location.

Acknowledgments
The data supporting the analysis and conclusions can be accessed at https://doi.org/10.5281/zenodo.1249433. This work was partly supported by the European Commission via projects ACTRIS and ACTRIS2, U.S. Department of Energy via the Office of Science (BER), and Academy of Finland via Center of Excellence in Atmospheric Sciences. M. Tuononen was supported by the Maj ja Tor Nesslingin Säätiö (grants 201500300 and 201600003). This work was also supported by the Academy of Finland Center of Excellence programme (grant 307331) and the U.S. Department of Energy (grant DE-SC0017338). Contribution to the instrumentation of JOYCE and its maintenance, as well as the funding of T. Marke, is realized by the Transregional Collaborative Research Center (TR32) *Patterns in Soil-Vegetation-Atmosphere Systems*, which is funded by the German Science Foundation (DFG).

References

Baars, H., Ansmann, A., Engelmann, R., & Althausen, D. (2008). Continuous monitoring of the boundary-layer top with lidar. *Atmospheric Chemistry and Physics*, *8*, 7281–7296. https://doi.org/10.5194/acp-8-7281-2008

Baklanov, A. A., Grisogono, B., Bornstein, R., Mahrt, L., Zilitinkevich, S. S., Taylor, P., et al. (2011). The nature, theory, and modeling of atmospheric planetary boundary layers. *Bulletin of the American Meteorological Society*, *92*, 123–128. https://doi.org/10.1175/2010BAMS2797.1

Banta, R. M., Pichugina, Y. L., & Brewer, W. A. (2006). Turbulent velocity-variance profiles in the stable boundary layer generated by a nocturnal low-level jet. *Journal of the atmospheric sciences*, *63*, 2700–2719.

Barlow, J. F., Dunbar, T. M., Nemitz, E. G., Wood, C. R., Gallagher, M. W., Davies, F., et al. (2011). Boundary layer dynamics over London, UK, as observed using Doppler lidar during REPARTEE-II. *Atmospheric Chemistry and Physics*, *11*, 2111–2125. https://doi.org/10.5194/acp-11-2111-2011

Bonin, T. A., Carroll, B. J., Hardesty, R. M., Brewer, W. A., Hajny, K., Salmon, O. E., & Shepson, P. B. (2018). Doppler lidar observations of the mixing height in Indianapolis using an automated composite fuzzy logic approach. *Journal of Atmospheric and Oceanic Technology*, *35*, 473–490. https://doi.org/10.1175/JTECH-D-17-0159.1, http://journals.ametsoc.org/doi/10.1175/JTECH-D-17-0159.1

Borque, P., Luke, E., & Kollias, P. (2016). On the unified estimation of turbulence eddy dissipation rate using Doppler cloud radars and lidars: Radar and lidar turbulence estimation. *Journal of Geophysical Research: Atmospheres*, *121*, 5972–5989. https://doi.org/10.1002/2015JD024543

Cuxart, J., & Jiménez, M. A. (2007). Mixing processes in a nocturnal low-level jet: An LES study. *Journal of the Atmospheric Sciences*, *64*, 1666–1679. https://doi.org/10.1175/JAS3903.1

Deardorff, J. W. (1972). Numerical investigation of neutral and unstable planetary boundary layers. *Journal of the Atmospheric Sciences*, *29*, 91–115. https://doi.org/10.1175/1520-0469(1972)029<0091:NIONAU>2.0.CO;2

Emeis, S., Schäfer, K., & Münkel, C. (2008). Surface-based remote sensing of the mixing-layer height — A review. *Meteorologische Zeitschrift*, *17*, 621–630. https://doi.org/10.1127/0941-2948/2008/0312

Frehlich, R., & Cornman, L. (2002). Estimating spatial velocity statistics with coherent Doppler lidar. *Journal of Atmospheric and Oceanic Technology*, *19*, 355–366. https://doi.org/10.1175/1520-0426-19.3.355

Fuentes, J. D., Chamecki, M., Nascimento dos Santos, R. M., Von Randow, C., Stoy, P. C., Katul, G., et al. (2016). Linking meteorology, turbulence, and air chemistry in the Amazon rain forest. *Bulletin of the American Meteorological Society*, *97*, 2329–2342. https://doi.org/10.1175/BAMS-D-15-00152.1

GDAS (2016). Global Data Assimilation System.

Garratt, J. (1994). Review: The atmospheric boundary layer. *Earth-Science Reviews*, *37*, 89–134. https://doi.org/10.1016/0012-8252(94)90026-4

Geerts, B., Parsons, D., Ziegler, C. L., Weckwerth, T. M., Biggerstaff, M. I., Clark, R. D., et al. (2017). The (2015), plains elevated convection at night field project. *Bulletin of the American Meteorological Society*, *98*, 767–786. https://doi.org/10.1175/BAMS-D-15-00257.1

Hari, P., & Kulmala, M. (2005). Station for measuring ecosystem-atmosphere relations (SMEAR II). *Boreal Environment Research*, *10*, 315–322.

Harvey, N. J., Hogan, R. J., & Dacre, H. F. (2013). A method to diagnose boundary-layer type using Doppler lidar: A method to diagnose boundary-layer type. *Quarterly Journal of the Royal Meteorological Society*, *139*, 1681–1693. https://doi.org/10.1002/qj.2068

Hirsikko, A., O'Connor, E. J., Komppula, M., Korhonen, K., Pfüller, A., Giannakaki, E., et al. (2014). Observing wind, aerosol particles, cloud and precipitation: Finland's new ground-based remote-sensing network. *Atmospheric Measurement Techniques*, *7*, 1351–1375. https://doi.org/10.5194/amt-7-1351-2014

Hogan, R. J., Grant, A. L. M., Illingworth, A. J., Pearson, G. N., & O'Connor, E. J. (2009). Vertical velocity variance and skewness in clear and cloud-topped boundary layers as revealed by Doppler lidar. *Quarterly Journal of the Royal Meteorological Society*, *135*, 635–643. https://doi.org/10.1002/qj.413

Holtslag, A. A. M., Svensson, G., Baas, P., Basu, S., Beare, B., Beljaars, A. C. M., et al. (2013). Stable atmospheric boundary layers and diurnal cycles: Challenges for weather and climate models. *Bulletin of the American Meteorological Society*, *94*, 1691–1706. http://journals.ametsoc.org/doi/abs/10.1175/BAMS-D-11-00187.1

ICAO (2005). Manual on low-level wind shear (Tech. Rep.). International Civil Aviation Organization.

Ibrahim, R., & Afshin, A. (2008). Solar position algorithm for solar radiation applications (Tech. Rep. NREL/TP-560-34302). National Renewable Energy Laboratory NREL.

Kaimal, J. C., & Finnigan, J. J. (1994). *Atmsopheric boundary layer flows: Their structure and measurement*. New York, NY: Oxford University Press.

Ketzler, G. (2014). The diurnal temperature cycle and its relation to boundary-layer structure during the morning transition. *Boundary-Layer Meteorology*, *151*, 335–351. https://doi.org/10.1007/s10546-013-9898-7, http://link.springer.com/10.1007/s10546-013-9898-7

Kleiner, A., Talwalkar, A., Sarkar, P., & Jordan, M. I. (2014). A scalable bootstrap for massive data. *Journal of the Royal Statistical Society: Series B (Statistical Methodology)*, *76*, 795–816. https://doi.org/10.1111/rssb.12050, http://doi.wiley.com/10.1111/rssb.12050

Krueger, S. K., McLean, G. T., & Fu, Q. (1995). Numerical simulation of the stratus-to-cumulus transition in the subtropical marine boundary layer. Part II: Boundary-layer circulation. *Journal of the Atmospheric Sciences*, *52*, 2851–2868. https://doi.org/10.1175/1520-0469(1995)052<2851:NSOTST>2.0.CO;2

Lothon, M., Lohou, F., Pino, D., Couvreux, F., Pardyjak, E. R., Reuder, J., et al. (2014). The BLLAST field experiment: Boundary-layer late afternoon and sunset turbulence. *Atmospheric Chemistry and Physics*, *14*, 10,931–10,960. https://doi.org/10.5194/acp-14-10931-2014, http://www.atmos-chem-phys.net/14/10931/2014/

Manninen, A. J., O'Connor, E. J., Vakkari, V., & Petäjä, T. (2016). A generalised background correction algorithm for a Halo Doppler lidar and its application to data from Finland. *Atmospheric Measurement Techniques*, *9*, 817–827. https://doi.org/10.5194/amt-9-817-2016

Moeng, C.-H., & Sullivan, P. P. (1994). A comparison of shear- and buoyancy-driven planetary boundary layer flows. *Journal of the Atmospheric Sciences*, *51*, 999–1022. https://doi.org/10.1175/1520-0469(1994)051<0999:ACOSAB>2.0.CO;2

Newsom, R. K., Brewer, W. A., Wilczak, J. M., Wolfe, D. E., Oncley, S. P., & Lundquist, J. K. (2017). Validating precision estimates in horizontal wind measurements from a Doppler lidar. *Atmospheric Measurement Techniques*, *10*, 1229–1240. https://doi.org/10.5194/amt-10-1229-2017

O'Connor, E. J., Hogan, R. J., & Illingworth, A. J. (2005). Retrieving stratocumulus drizzle parameters using Doppler radar and lidar. *Journal of Applied Meteorology*, *44*, 14–27.

O'Connor, E. J., Illingworth, A. J., Brooks, I. M., Westbrook, C. D., Hogan, R. J., Davies, F., & Brooks, B. J. (2010). A method for estimating the turbulent kinetic energy dissipation rate from a vertically pointing Doppler lidar, and independent evaluation from balloon-borne in situ measurements. *Journal of Atmospheric and Oceanic Technology*, *27*, 1652–1664. https://doi.org/10.1175/2010JTECHA1455.1

Oke, T. R. (1992). Boundary layer climates, Routledge, London; New York, 2nd edn.

Pal, S., Lopez, M., Schmidt, M., Ramonet, M., Gibert, F., Xueref-Remy, I., & Ciais, P. (2015). Investigation of the atmospheric boundary layer depth variability and its impact on the 222 Rn concentration at a rural site in France: Impact of ABL depth variability on radon. *Journal of Geophysical Research: Atmospheres*, *120*, 623–643. https://doi.org/10.1002/2014JD022322

Päschke, E., Leinweber, R., & Lehmann, V. (2015). An assessment of the performance of a 1.5 µm Doppler lidar for operational vertical wind profiling based on a 1-year trial. *Atmospheric Measurement Techniques*, *8*, 2251–2266. https://doi.org/10.5194/amt-8-2251-2015

Pearson, G., Davies, F., & Collier, C. (2009). An analysis of the performance of the UFAM pulsed Doppler lidar for observing the boundary layer. *Journal of Atmospheric and Oceanic Technology*, *26*, 240–250. https://doi.org/10.1175/2008JTECHA1128.1

Pearson, G., Davies, F., & Collier, C. (2010). Remote sensing of the tropical rain forest boundary layer using pulsed Doppler lidar. *Atmospheric Chemistry and Physics*, *10*, 5891–5901. https://doi.org/10.5194/acp-10-5891-2010

Rimoldini, L. (2014). Weighted skewness and kurtosis unbiased by sample size and Gaussian uncertainties. *Astronomy and Computing*, *5*, 1–8. https://doi.org/10.1016/j.ascom.2014.02.001, http://linkinghub.elsevier.com/retrieve/pii/S2213133714000092

Rye, B. J., & Hardesty, R. M. (1993). Discrete spectral peak estimation in incoherent backscatter heterodyne lidar. I. Spectral accumulation and the Cramer-Rao lower bound. *Geoscience and Remote Sensing, IEEE Transactions on*, *31*, 16–27. https://doi.org/10.1109/36.210440

Schween, J. H., Hirsikko, A., Löhnert, U., & Crewell, S. (2014). Mixing-layer height retrieval with ceilometer and Doppler lidar: From case studies to long-term assessment. *Atmospheric Measurement Techniques*, *7*, 3685–3704. https://doi.org/10.5194/amt-7-3685-2014

Smalikho, I. N., & Banakh, V. A. (2017). Measurements of wind turbulence parameters by a conically scanning coherent Doppler lidar in the atmospheric boundary layer. *Atmospheric Measurement Techniques*, *10*, 4191–4208. https://doi.org/10.5194/amt-10-4191-2017

Su, J., Felton, M., Lei, L., McCormick, M. P., Delgado, R., & St. Pé, A. (2016). Lidar remote sensing of cloud formation caused by low-level jets: Cloud formation caused by low-level jets. *Journal of Geophysical Research: Atmospheres*, *121*, 5904–5911. https://doi.org/10.1002/2015JD024590

Träumner, K., Kottmeier, C., Corsmeier, U., & Wieser, A. (2011). Convective boundary-layer entrainment: Short review and progress using Doppler lidar. *Boundary-Layer Meteorology*, *141*, 369–391. https://doi.org/10.1007/s10546-011-9657-6

Tucker, S. C., Senff, C. J., Weickmann, A. M., Brewer, W. A., Banta, R. M., Sandberg, S. P., et al. (2009). Doppler lidar estimation of mixing height using turbulence, shear, and aerosol profiles. *Journal of Atmospheric and Oceanic Technology*, *26*, 673–688. https://doi.org/10.1175/2008JTECHA1157.1

Tuononen, M., O'Connor, E. J., Sinclair, V. A., & Vakkari, V. (2017). Low-level jets over Utö, Finland, based on Doppler lidar observations. *Journal of Applied Meteorology and Climatology*, *56*, 2577–2594. https://doi.org/10.1175/JAMC-D-16-0411.1

Vakkari, V., O'Connor, E. J., Nisantzi, A., Mamouri, R. E., & Hadjimitsis, D. G. (2015). Low-level mixing height detection in coastal locations with a scanning Doppler lidar. *Atmospheric Measurement Techniques*, *8*, 1875–1885. https://doi.org/10.5194/amt-8-1875-2015

Westbrook, C. D., Illingworth, A. J., O'Connor, E. J., & Hogan, R. J. (2010). Doppler lidar measurements of oriented planar ice crystals falling from supercooled and glaciated layer clouds. *Quarterly Journal of the Royal Meteorological Society*, *136*, 260–276. https://doi.org/10.1002/qj.528

Wood, R. (2012). Stratocumulus clouds. *Monthly Weather Review*, *140*, 2373–2423. https://doi.org/10.1175/MWR-D-11-00121.1